Molecular Biology Research Communications 2026;15(3):145-158 DOI:10.22099/mbrc.2026.55232.2260

Original Article MBRC Open Access

Steroids from *Talaromyces stipitatus* as potential hepatocellular carcinoma inhibitors: A computational study

Hung Duc Nguyen*

Faculty of Biology, Thai Nguyen University of Education, 24000, Thai Nguyen, Vietnam

ABSTRACT

Hepatocellular carcinoma frequently exhibits evasion of apoptosis, rendering the anti-apoptotic Bcl-2 protein a pertinent therapeutic target. Steroids from *Talaromyces stipitatus* were evaluated as Bcl-2 inhibitors using molecular docking, molecular dynamics simulation, MMGBSA free-energy estimation, ADMET prediction, and DFT descriptors. Docking prioritized CPD2 over Paclitaxel. It also indicated accommodation within a conserved pocket supported by hydrogen-bond and hydrophobic interactions. Molecular dynamics suggested sustained stability and compactness for the CPD2-Bcl-2 complex. In contrast, the reference complex exhibited comparatively larger conformational excursions. MMGBSA favored CPD2, with improved net association attributable primarily to a reduced solvation penalty. ADMET profiling indicated limited aqueous solubility and a shared hERG II liability, while predicting no hepatotoxicity alert for CPD2. DFT descriptors were consistent with higher electronic responsiveness for CPD2 relative to the reference. These findings suggest that CPD2 may serve as a promising scaffold for developing Bcl-2-targeted therapeutic strategies against HCC. Future in vitro and in vivo studies are required to validate these computational predictions and guide lead optimization.

Keywords: Anti-apoptosis; Bcl-2; DFT; Hepatocellular carcinoma; Molecular docking; *Talaromyces stipitatus*.

INTRODUCTION

According to cancer statistics, liver cancer remains a major global malignancy, with approximately 865,269 new cases and 757,948 deaths reported worldwide, ranking 6th in incidence and 3rd in cancer-related mortality [1]. Its high mortality is associated with chronic infections, excessive alcohol consumption, metabolic diseases, late-stage diagnosis, and regional disparities in disease burden [2, 3]. Hepatocellular carcinoma (HCC) is the most common type of primary liver cancer, making up the vast majority (75-85%) of liver cancer cases [4]. For early-stage HCC, surgical resection, ablation, and liver transplantation are primary curative treatments, aiming for long-term survival, often achieving over 5-year survival rates, with liver transplant offering the best outcomes but limited by donor availability, while ablation and resection are standard for localized tumors, though resection might offer better disease-free survival in some cases [5, 6]. Apoptosis, or programmed cell death, is crucial for

*Corresponding Authors: Faculty of Biology, Thai Nguyen University of Education, 24000, Thai Nguyen, Vietnam; Fax: +84 2083857867; Email: hungnd@tnue.edu.vn

pISSN 2322-181X eISSN 2345-2005

removing damaged cells, but cancer cells evade this process, allowing uncontrolled growth. In HCC, dysregulated apoptosis contributes to tumor survival, disease progression, and resistance to therapy [7]. Bcl-2 proteins are key regulators of cell death, and their overexpression helps liver cancer cells survive, promoting tumor growth and resistance to chemotherapy [8, 9]. Accordingly, inhibition of anti-apoptotic Bcl-2 proteins may re-establish apoptotic signaling and mitigate resistance to conventional chemotherapeutic and radiotherapeutic regimens in HCC [10].

Natural products from plant and microbial sources provide structurally diverse bioactive scaffolds that may act through complementary mechanisms relevant to cancer therapy. This multi-target approach is beneficial for managing complex conditions, such as cancer, inflammation, or infection, as it can address multiple pathological processes simultaneously, improve efficacy, and potentially reduce toxicity [11]. Among those compounds, steroids are vital in oncology, acting both as direct anti-cancer drugs and for managing cancer symptoms or treatment side effects [12]. In this context, fungal steroidal metabolites represent a relevant extension of natural-product-based anticancer discovery. Building on the multi-target potential of natural products and the recognized relevance of steroids in oncology, attention has increasingly shifted toward microbial sources, particularly filamentous fungi, as reservoirs of steroidal metabolites with anticancer activity. *Talaromyces stipitatus* is a filamentous fungus closely related to Penicillium, typically considered non-pathogenic, and is known for producing various bioactive compounds. A previous study on this species led to the isolation of steroids with anti-hepatocellular carcinoma activity against the Hep3B cancer cell line [13]. Nonetheless, the mechanistic determinants underlying this activity, particularly with respect to signaling networks governed by central apoptotic regulators, remain incompletely resolved. In response, an integrated in silico study was conducted to elucidate plausible molecular mechanisms using complementary computational approaches, including molecular docking, molecular dynamics simulations, MM-GBSA free energy estimation, ADMET profiling, and DFT-based electronic analysis. Taken together, the findings provide a scientific basis for subsequent experimental verification and lead optimization toward hepatocellular carcinoma therapeutics, while emphasizing that definitive efficacy and safety characterization requires further in vitro and in vivo evaluation.

MATERIALS AND METHODS

Structural preparation of selected ligands: These selected iridoids, including (22*E*,24*R*)-3*β*,5*α*-dihydroxy-14*β*,15*β*-epoxyergosta-7,22-diene-6-one (CPD1), (22*E*,24*R*)-9*α*,15*α*-dihydroxyergosta-4,6,8(14),22-tetraen-3-one (CPD2), 15R, 20*R*,24*R*, $\Delta^{4,6,8(14),22}$-tetraene-3-one-ergosterol (CPD3), have molecular formulas of $C_{28}H_{40}O_3$, $C_{28}H_{42}O_4$, $C_{28}H_{42}O_2$, respectively, with molecular weights of 424.2977, 442.3083, 408.3028 *m/z*. Paclitaxel, possessing a molecular formula of $C_{47}H_{51}NO_{14}$ and a molecular weight of 853.3310 *m/z*, was chosen as the positive control (Fig. 1).

Molecular docking: Three-dimensional conformations of the selected steroidal ligands were generated in BIOVIA Discovery Studio Visualizer and saved as PDB files. Ligand preparation involved the addition of polar hydrogen atoms, assignment of Gasteiger partial charges, and specification of rotatable bonds as flexible torsions. The Bcl-2 structure (PDB ID: 6O0K) was obtained from the RCSB Protein Data Bank in PDB format [14]. Molecular docking was executed in AutoDock Tools using a 60 × 60 × 60 grid with 0.375 Å spacing, centered at x = -10.843 Å, y = 1.749 Å, and z = -9.661 Å. Conformational search and scoring relied on the Lamarckian genetic algorithm to prioritize low-energy binding orientations associated with stable interaction profiles. The highest-ranked pose for each ligand was subsequently analyzed in Discovery Studio Client 2024 and evaluated against the Paclitaxel docking pose on the same receptor to determine agreement in binding mode and key intermolecular contacts [15].

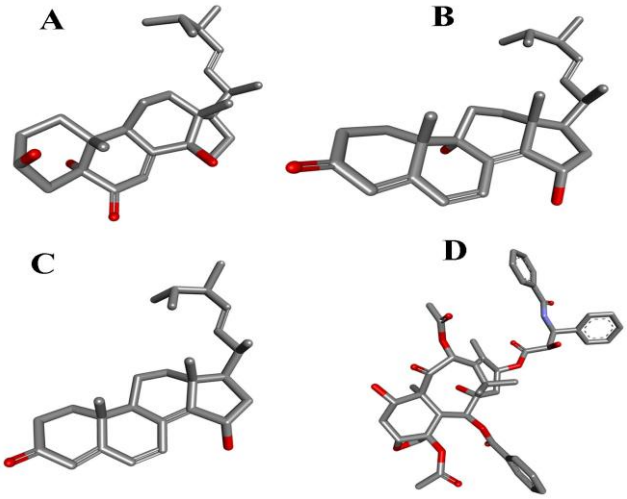

Figure 1: 3D Structures of selected ligands. (A) CPD1, (B) CPD2, (C) CPD3, (D) Paclitaxel.

Molecular dynamics simulation: Molecular dynamics simulations were carried out for the Bcl-2-ligand complex (PDB ID: 6O0K) using the highest-scoring docking pose as the initial configuration, with a simulation length of 100 ns in GROMACS 2024.4 [16]. Before dynamics, the protein model was curated in Swiss-PdbViewer by rebuilding absent residues and atoms [17]. Ligand force-field parameters were obtained via SwissParam [18]. The complex was solvated in a triclinic SPC water box and supplemented with 0.15 M NaCl to approximate physiological ionic strength. Energy minimization was performed for 50,000 steps to remove unfavorable contacts and relax electrostatic interactions. Equilibration employed a two-step scheme consisting of 100 ps under NVT conditions followed by 100 ps under NPT conditions, maintained at 300 K and 1 bar. Production runs were executed in triplicate, with each replicate spanning 100 ns and a 2 fs integration step. Trajectory coordinates, energies, and log files were saved every 10 ps during the production simulations. Representative configurations were extracted at 10 ns intervals for structural inspection. Trajectories were analyzed in Grace to quantify root mean square deviation (RMSD), root mean square fluctuation (RMSF), radius of gyration (Rg), number of hydrogen bonds, and solvent-accessible surface area (SASA). Conformational stability across simulations was further examined through structural superimposition in UCSF Chimera 1.13.3 [19]. To evaluate interaction persistence, ligand poses at 0 ns and 100 ns were aligned within the binding cavity, allowing for the assessment of the continuity of key contacts, including hydrogen bonding, van der Waals interactions, and hydrophobic contributions, throughout the 100 ns trajectory.

Molecular mechanics generalised Born surface area (MMGBSA) analysis: Binding free energies for the CPD2-6O0K and Paclitaxel-6O0K complexes were estimated with the gmx_MMPBSA workflow under the charmm36 force field. The polar term of the solvation free energy was evaluated using a generalized Born implicit solvent representation, whereas the non-polar contribution was derived from solvent-accessible surface area calculations. Calculations utilized an ensemble of conformations obtained from molecular dynamics trajectories spanning a 20-100 ns window (totaling 80 ns), comprising 125 evenly distributed snapshots collected every 80 ps. This frame-based protocol supported a quantitative comparison of the interaction energetics of the two ligands, thereby clarifying relative binding affinities and the energetic consistency of each complex across the sampled simulation interval [20].

Assay protocol for ADMET prediction: Early appraisal of ADMET characteristics is crucial for anticipating pharmacokinetic liabilities and safety risks during drug discovery, thereby reducing downstream failure rates and enhancing the selection of candidates with appropriate therapeutic potential. Here, the pkCSM platform was applied to predict the ADMET profiles of CPD2 and Paclitaxel. This framework leverages graph-based molecular descriptors

to infer absorption, distribution, metabolism, excretion, and toxicity parameters, enabling a structured comparison of key developability attributes for the evaluated compounds.

Quantum chemistry computation using the Density Functional Theory (DFT) method: Geometry optimisation of CPD2 and Paclitaxel was conducted with the ORCA quantum chemistry package (v6.1.0). Starting coordinates were generated in Avogadro, whereas molecular orbital inspection and associated electronic analyses were performed in IboView (v20211019) [21-23]. Density functional theory computations used the B3LYP exchange-correlation functional in conjunction with the 6-31G(d,p) basis set to obtain converged electronic wavefunctions. Using the final optimised structures, quantum-chemical descriptors were determined, including the highest occupied molecular orbital (HOMO) energy, the lowest unoccupied molecular orbital (LUMO) energy, the HOMO-LUMO gap (ΔE), chemical potential (μ), electronegativity (χ), global hardness (η), softness (σ), and electrophilicity index (ω). These reactivity indices were interpreted under the Koopmans' theorem framework to describe electronic characteristics and anticipated chemical behaviour of the investigated compounds [24, 25].

RESULTS AND DISCUSSION

Molecular docking is an in silico approach used to model the association between a small molecule ligand and a macromolecular receptor, typically a protein. The method estimates the preferred three-dimensional binding pose within a putative site, evaluates binding affinity through scoring functions, and characterizes key intermolecular contacts that contribute to complex stabilization. By providing atomic-level hypotheses for recognition and energetics, docking supports structure-guided drug discovery through prioritization of candidate compounds and mechanistic interpretation of ligand-target interactions [26]. As summarized in Table 1, docking-derived affinities and residue-level interaction patterns were examined for three steroidal candidates (CPD1-CPD3) against Bcl-2 (PDB ID: 6O0K), with Paclitaxel included as a reference ligand.

Table 1: The interactions between the docked ligands and the protein 6O0K.

	Binding energy (kJ/mol)	Hydrogen bond	Van der Waals force	Hydrophobic interaction
CPD1	-9.10	Glu136	Asp111, Phe138, Arg139, Asp140, Arg146, Ala149, Glu152, Phe153	Phe104, Phe112, Met115, Leu137, Val156
CPD2	-10.07	Asp111, Phe112, Ala149	Tyr108, Val133, Glu136, Asp140, Arg146, Glu152, Phe153, Val156	Phe104, Met115, Leu137, Arg139, Ala149
CPD3	-9.98	Asp111, Phe112	Tyr108, Val133, Glu136, Asp140, Arg146, Glu152, Phe153, Phe153, Val156	Phe104, Met115, Leu137, Ala149
Paclitaxel	-6.80	Asn143, Gly145, Arg146	Ala100, Asp103, Arg107, Tyr108, Asp111, Leu137, Trp144, Phe198	Phe104, Glu136, Arg139, Asp140, Val148, Ala149, Tyr202

Across the steroid series, the binding cavity was consistently delineated by recurrent residues, most prominently Phe104, Tyr108, Asp111, Met115, Leu137, Ala149, Glu152, and Phe153, indicating convergence toward a shared recognition region. Non-covalent stabilization in such complexes is typically supported by complementary forces. Directional hydrogen bonding helps constrain ligand orientation, whereas hydrophobic packing reduces solvent exposure within the pocket. In addition, short-range dispersion and van der Waals

complementarity refine geometric fit and contribute incrementally to association energetics [27, 28]. Predicted binding energies for the steroidal ligands ranged from -10.07 to -9.10 kcal/mol, whereas Paclitaxel exhibited a less favorable value (-6.80 kcal/mol) under the same docking protocol, suggesting weaker stabilization relative to CPD1-CPD3. Among the tested steroids, CPD2 produced the most favorable affinity (-10.07 kcal/mol) and occupied a pocket framed by Phe104, Tyr108, Asp111, Met115, Leu137, Ala149, Glu152, and Phe153. Hydrogen-bond formation was annotated with Asp111, Phe112, and Ala149, consistent with a mixed polar-nonpolar binding architecture in which polar anchoring complements aromatic/aliphatic enclosure (Fig. 2A). CPD3 showed a closely related binding site usage (Phe104, Tyr108, Asp111, Met115, Leu137, Ala149, Glu152, Phe153) and an affinity of -9.98 kcal/mol, with hydrogen bonds involving Asp111 and Phe112, supporting a similar anchoring strategy but with slightly reduced predicted stabilization compared with CPD2. CPD1 yielded the least favorable affinity among the steroidal candidates (-9.10 kcal/mol) while retaining contacts with core pocket residues (Phe104, Asp111, Met115, Leu137, Ala149, Glu152, Phe153); a hydrogen bond to Glu136 was observed, indicating an alternative polar interaction pattern relative to CPD2/CPD3.

In contrast, Paclitaxel engaged a broader residue set extending beyond the core steroid-recognition region, including Asp103, Arg107, Asn143, Trp144, Val148, Phe198, and Tyr202. It formed hydrogen bonds with Asn143, Gly145, and Arg146 (Fig. 2B). Despite this expanded interaction footprint, the docking score remained less favorable (-6.80 kcal/mol), implying that the sampled pose provided lower predicted energetic complementarity than the steroidal candidates in this binding environment.

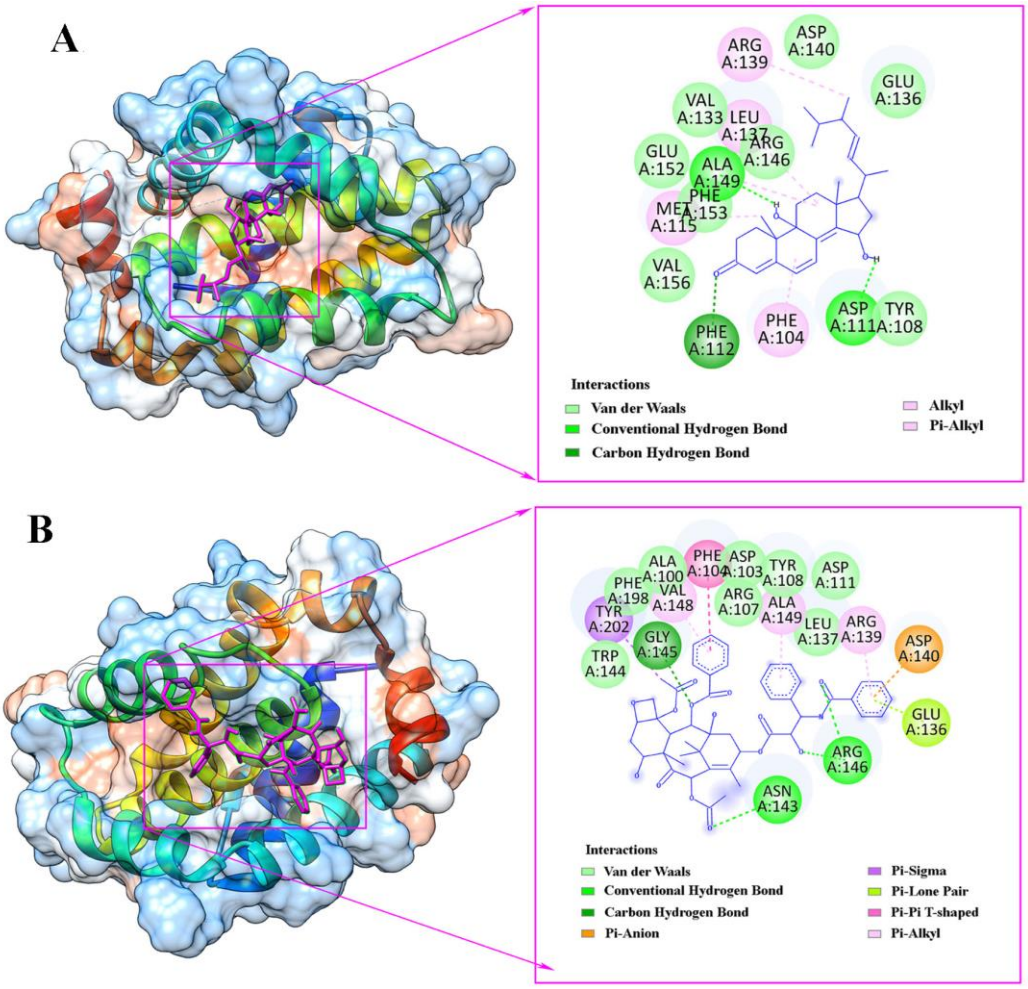

Figure 2: Molecular docking model and 2D interaction diagram of CPD2 (A), and Paclitaxel (B) with 6O0K protein.

Collectively, the docking results indicate that the most negative binding energies coincided with engagement of the conserved pocket residues (Phe104, Tyr108, Asp111, Met115, Leu137, Ala149, Glu152, Phe153) together with hydrogen-bond anchoring involving Asp111 and Phe112 (and Ala149 for CPD2). On this basis, CPD2 represents the leading candidate for subsequent molecular dynamics simulations to evaluate conformational stability and persistence of the key contacts within an explicit-solvent, fully flexible protein environment.

Molecular dynamics simulations are a central component of contemporary structure-based drug discovery, providing time-resolved, atomistic descriptions of ligand-target systems. This approach enables assessment of binding-mode stability, characterization of protein conformational plasticity, and identification of transient pockets and allosteric regions that may be inaccessible to static structures. By complementing experimental observations with mechanistic insight into interaction persistence and dynamic coupling, molecular dynamics supports optimization of lead candidates and expedites the development of therapeutics with improved efficacy [29]. Therefore, the evaluation systematically investigated RMSD, RMSF, Rg, Hbonds, and SASA metrics to determine the stability, flexibility, and solvent exposure of the CPD2-6O0K and Paclitaxel-6O0K complexes throughout the simulation [30]. Consequently, The total and potential energy values were -242,355 and -300,627 kJ/mol for CPD2-6O0K, and -240,117 and -298,327 kJ/mol for Paclitaxel-6O0K, respectively.

Root mean square deviation (RMSD) provides a time-dependent measure of structural departure from a reference conformation after optimal superposition. It is commonly used to evaluate whether a protein-ligand system attains a stable dynamical regime. In the present trajectories (Fig. 3A), both complexes exhibited an initial relaxation during the early nanoseconds, after which the RMSD values remained confined to a narrow interval without progressive drift across the 100-ns window. The CPD2-6O0K complex largely fluctuated around 0.16-0.21 nm, whereas the Paclitaxel-6O0K complex occupied a comparable range but displayed a modestly elevated band during approximately the mid-to-late segment of the simulation, with excursions approaching 0.23-0.24 nm. The absence of sustained upward trends supports preservation of the global fold under both bound states. At the same time, the slightly lower RMSD band observed for CPD2 is consistent with marginally reduced deviation relative to the reference structure.

Root mean square fluctuation (RMSF) quantifies residue-resolved mobility around the mean position and highlights flexible segments that contribute to local dynamical heterogeneity [31]. The RMSF profiles for CPD2-6O0K and Paclitaxel-6O0K (Fig. 3B) showed broadly similar patterns, with low-amplitude fluctuations across most of the sequence and several localized peaks. The Paclitaxel-bound system displayed higher maxima at prominent flexible regions, reaching 0.20 nm in the major peak near the central portion of the profile. In contrast, the corresponding peak in the CPD2 complex remained lower (approximately 0.14-0.15 nm). Additional peaks of moderate amplitude were observed in both systems, indicating that ligand binding influenced the magnitude of motions in selected segments without inducing widespread destabilization.

The radius of gyration (Rg) reports the mass-weighted spatial dispersion of atoms around the center of mass and is used to monitor overall compactness [32]. As shown in Figure 3C, both complexes maintained Rg values within a restricted band (1.41-1.46 nm) throughout the trajectory, indicating a stable global architecture. A subtle separation between traces was evident over extended intervals, with the Paclitaxel-6O0K complex tending toward slightly lower Rg values than CPD2-6O0K, suggesting a marginally more compact ensemble for the Paclitaxel-bound state. However, the difference remained small and did not reflect large-scale expansion.

Hydrogen-bond counts provide a direct indicator of polar contact formation and persistence at the protein-ligand interface. The hydrogen-bond time series (Fig. 3D) indicated limited and intermittent hydrogen bonding for CPD2-6O0K, with the trajectory dominated by 0-1 hydrogen bond and occasional brief events reaching 2. In contrast, Paclitaxel-6O0K demonstrated a broader distribution, frequently sampling 0-2 hydrogen bonds and exhibiting transient clusters

in which the count increased to 3-4, notably around the mid-trajectory region and again near the simulation endpoint. This pattern suggests more extensive, yet episodic, polar anchoring for Paclitaxel, whereas CPD2 appears to rely less on sustained hydrogen-bond networks.

Solvent-accessible surface area (SASA) reflects solvent exposure and can indirectly report changes in packing and conformational openness [33]. The SASA traces (Fig. 3E) remained stable for both systems, predominantly spanning 80-89 nm² with no persistent monotonic drift, supporting maintained structural integrity. Across most of the simulation, the CPD2-6O0K complex showed a slightly lower SASA envelope than the Paclitaxel-6O0K complex, consistent with modestly reduced solvent exposure under CPD2 binding.

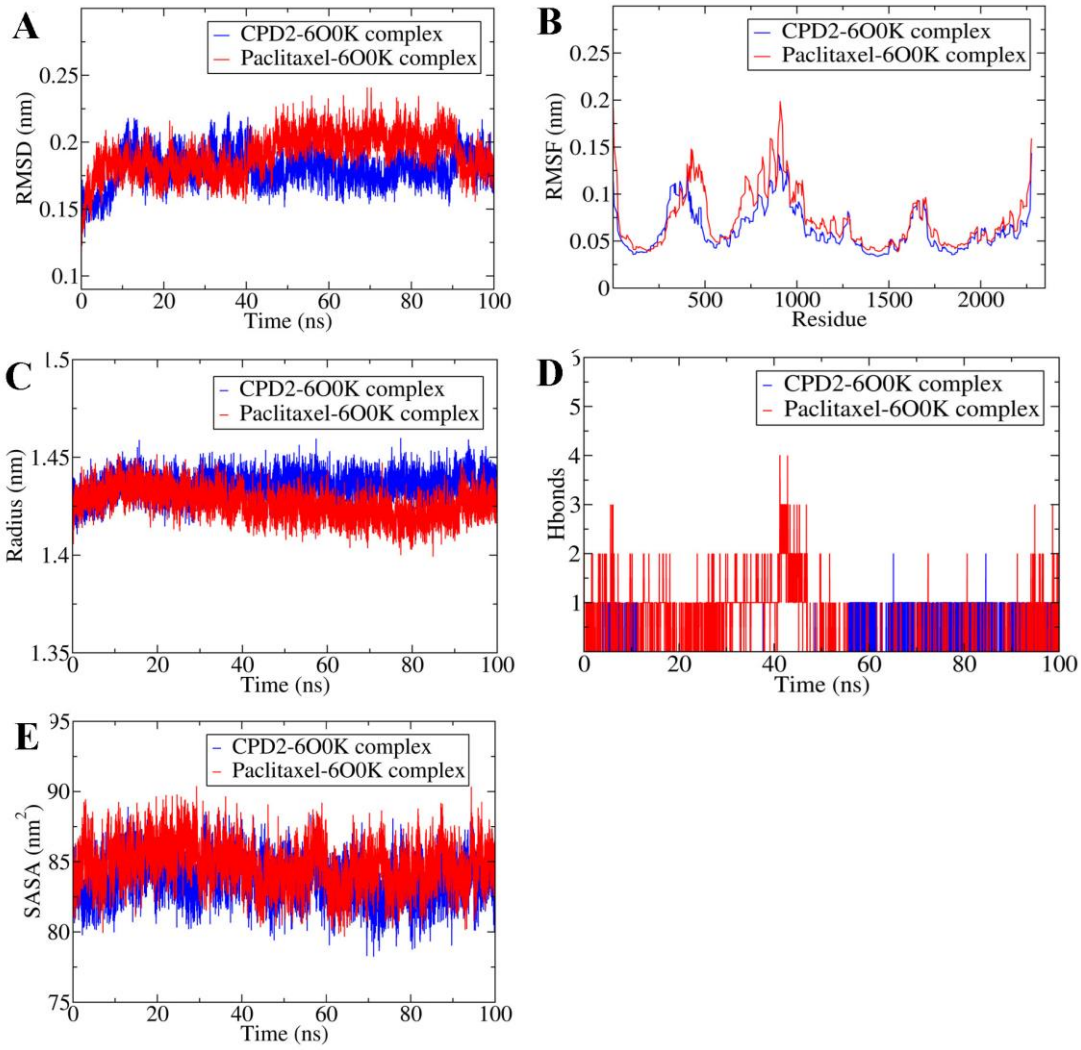

Figure 3: HOMO and LUMO surface diagrams of CPD2 (A) and Paclitaxel (B). Results of MD simulation for the bindings of CPD2 (blue) and Paclitaxel (red) with 6O0K protein. (A) RMSD, (B) RMSF, (C) Rg, (D) Hbonds, (E) SASA.

Collectively, RMSD, RMSF, Rg, hydrogen-bonding, and SASA readouts support stable dynamics for both CPD2-6O0K and Paclitaxel-6O0K over 100 ns. Rather than indicating major destabilization in either system, the comparative profiles suggest a modestly more restrained dynamic behavior for CPD2-6O0K, whereas Paclitaxel-6O0K exhibited more frequent but transient high-count hydrogen-bond episodes.

Molecular Mechanics with Generalized Born Surface Area (MMGBSA) is a commonly applied computational framework for approximating ligand-receptor binding free energies, particularly in structure-based drug discovery. The method decomposes binding energetics into molecular mechanics interaction terms and implicit-solvent contributions described by a

generalized Born model combined with a surface-area term for nonpolar solvation. This partitioning provides a pragmatic compromise between computational efficiency and predictive utility for macromolecular complexes. However, accuracy remains sensitive to methodological choices such as dielectric treatment, force-field parametrization, trajectory sampling, and the handling of entropic effects [34]. Binding free energies for the CPD2-6O0K and Paclitaxel-6O0K complexes were quantified using the MMGBSA formalism, in which the binding term is defined as ΔG_bind = G_complex - (G_receptor + G_ligand). Although a complete thermodynamic description may be expressed as ΔG_bind = ΔH - TΔS, exclusion of the entropic term yields an enthalpy-weighted estimate that remains suitable for comparative ranking within a consistent setup. Therefore, the MMGBSA values should be interpreted primarily as relative binding estimates rather than absolute binding free energies, and conclusions are restricted to comparisons between CPD2 and Paclitaxel under the same computational protocol. Energy decomposition separates gas-phase interactions (ΔG_GAS = ΔVDWAALS + ΔEEL) from solvation effects (ΔG_SOLV = ΔEGB + ΔESURF), enabling interpretation of the dominant stabilizing and penalizing contributions.

As reported in Table 2, both complexes exhibit a favorable association, reflected by negative ΔTOTAL values. CPD2-6O0K displays ΔTOTAL = -35.68 ± 2.88 kcal/mol, whereas Paclitaxel-6O0K shows ΔTOTAL = -29.75 ± 3.34 kcal/mol, indicating a more favorable mean binding estimate for CPD2 by 5.93 kcal/mol. The partitioning of terms reveals contrasting energetic drivers. Paclitaxel presents a markedly stronger gas-phase contribution (ΔG_GAS = -63.53 ± 8.01 kcal/mol) than CPD2 (ΔG_GAS = -44.58 ± 4.48 kcal/mol), supported by more favorable van der Waals interactions (ΔVDWAALS = -47.45 ± 3.38 vs. -43.65 ± 2.38 kcal/mol) and substantially stronger electrostatics (ΔEEL = -16.08 ± 6.87 vs. -0.92 ± 4.22 kcal/mol).

Table 2: Free energy of binding obtained using MMGBSA calculations.

Energy Component	Average (kcal/mol)		Standard Deviation	
	CPD2-6O0K	Paclitaxel-6O0K	CPD2-6O0K	Paclitaxel-6O0K
ΔVDWAΔALS	-43.65	-47.45	2.38	3.38
ΔEEL	-0.92	-16.08	4.22	6.87
ΔEGB	14.3	40.07	3.47	6.43
ΔESURF	-5.4	-6.29	0.3	0.45
ΔGGAS	-44.58	-63.53	4.48	8.01
ΔGSOLV	8.9	33.78	3.41	6.22
ΔTOTAL	-35.68	-29.75	2.88	3.34

Despite this advantage in the gas phase, Paclitaxel incurs a pronounced solvation penalty (ΔG_SOLV = 33.78 ± 6.22 kcal/mol) relative to CPD2 (ΔG_SOLV = 8.90 ± 3.41 kcal/mol). This difference is primarily attributable to the polar solvation term, with ΔEGB = 40.07 ± 6.43 kcal/mol for Paclitaxel compared with 14.30 ± 3.47 kcal/mol for CPD2, indicating substantially more substantial electrostatic desolvation costs for the reference ligand. The nonpolar solvation component is comparable in magnitude between systems (ΔESURF = -6.29 ± 0.45 kcal/mol for Paclitaxel; -5.40 ± 0.30 kcal/mol for CPD2) and therefore contributes minimally to the observed separation in ΔTOTAL.

Variability across the trajectory is modest for both complexes. However, Paclitaxel exhibits consistently higher dispersions across several terms (notably ΔEEL, ΔEGB, ΔG_GAS, and ΔG_SOLV), culminating in a larger ΔTOTAL standard deviation (3.34 vs. 2.88 kcal/mol). Overall, the MMGBSA results indicate that CPD2 achieves a more favorable net binding free energy by substantially reducing solvation penalties, which outweigh Paclitaxel's stronger gas-phase interactions.

In drug discovery, ADMET prediction utilizes computational models, including machine learning and related data-driven approaches, to estimate absorption, distribution, metabolism, excretion, and toxicity properties at an early stage. Such forecasts provide a preliminary appraisal of developability before resource-intensive experimental evaluation. They integrate indicators of systemic exposure, target-site access, metabolic liability, clearance routes, and

safety-relevant risks. By anticipating pharmacokinetic behavior and potential toxicities, this strategy facilitates the early de-prioritization of high-risk compounds and guides lead optimization, thereby enhancing the efficiency of selecting candidates with more favorable efficacy-safety profiles [35]. In silico ADMET profiling was conducted to compare the predicted pharmacokinetic behavior and safety-related alerts of CPD2 with those of the reference compound, Paclitaxel. The evaluated descriptors were organized under absorption, distribution, metabolism, excretion, and toxicity (Table 3). This comparative assessment provides an initial basis for identifying developability constraints relevant to computational screening of Bcl-2-targeting candidates.

Table 3: Predicted ADMET properties of CPD2 and Paclitaxel

ADMET properties	Unit	CPD2	Paclitaxel
Water Solubility	(Log mol/L)	(log mol/L)	-6.015
Caco2 permeability	(Log Papp in 10-6 cm/s)	(log Papp in 10-6 cm/s)	1.235
Intestinal absorption (Human)	(% Absorbed)	(% Absorbed)	93.986
Skin permeability	(Log Kp)	(log Kp)	-3.474
P-glycoprotein substrate	Yes/No	Yes/No	Yes
P-glycoprotein I inhibitor	Yes/No	Yes/No	Yes
P-glycoprotein II inhibitor	Yes/No	Yes/No	Yes
VDss	(Log L/kg)	0.796	1.458
Fraction unbound (human)	(Fu)	0.075	0
BBB permeability	(Log BB)	0.147	-1.731
CNS permeability	(Log PS)	-1.714	-3.85
CYP2D6 substrate	Yes/No	No	No
CYP3A4 substrate	Yes/No	Yes	Yes
CYP1A2 inhibitor	Yes/No	No	No
CYP2C19 inhibitor	Yes/No	No	No
CYP2C9 inhibitor	Yes/No	No	No
CYP2D6 inhibitor	Yes/No	No	No
CYP3A4 inhibitor	Yes/No	No	Yes
Total clearance	(Log ml/min/kg)	0.505	-0.36
Renal OCT2 substrate	Yes/No	No	No
AMES toxicity	Yes/No	No	No
Max. tolerated dose (human)	(Log mg/kg/day)	-0.085	0.199
hERG I inhibitor	Yes/No	No	No
hERG II inhibitor	Yes/No	Yes	Yes
Oral rat acute toxicity (LD50)	(mol/kg)	2.25	2.776
Oral rat chronic toxicity (LOAEL)	(Log mg/kg_bw/day)	1.76	3.393
Hepatotoxicity	Yes/No	No	Yes
Skin sensation	Yes/No	No	No
T. Pyriformis toxicity	(Log ug/L)	0.864	0.285
Minnow toxicity	(Log mM)	-0.823	2.988

For absorption-related endpoints, CPD2 exhibited markedly lower predicted aqueous solubility than Paclitaxel (water solubility: -6.015 vs -3.518 log mol/L), indicating a more substantial dissolution limitation under the applied model. In contrast, CPD2 showed higher predicted epithelial permeability (Caco2 permeability: 1.235 vs 0.623 log Papp in 10^{-6} cm/s) while retaining high predicted human intestinal absorption (93.986% vs 100%). Dermal permeation was expected to be lower for CPD2, as reflected by a more negative skin permeability value (-3.474 vs -2.735 log Kp). Transporter annotations were concordant between compounds, with both classified as P-glycoprotein substrates and as inhibitors of P-glycoprotein I and II.

Distribution parameters indicated divergent systemic disposition tendencies. The predicted steady-state volume of distribution was lower for CPD2 than for Paclitaxel (VDss: 0.796 vs 1.458 log L/kg), suggesting comparatively reduced tissue distribution for CPD2 within this framework. Plasma protein binding predictions also differed, as CPD2 retained a measurable

unbound fraction (Fu = 0.075), whereas Paclitaxel was reported as Fu = 0. Central exposure indices favored higher predicted brain penetration for CPD2, with BBB permeability (log BB: 0.147 vs -1.731) and CNS permeability (log PS: -1.714 vs -3.85) indicating less restrictive CNS access for CPD2 than for Paclitaxel.

Metabolism-related predictions were broadly similar, with neither compound categorized as a CYP2D6 substrate and both annotated as CYP3A4 substrates. Inhibition flags across major CYP isoforms were largely absent for CPD2. In contrast, Paclitaxel was predicted to inhibit CYP3A4, indicating a higher potential for CYP3A4-mediated interaction liability for the reference compound under the same predictor.

Excretion estimates suggested higher predicted clearance for CPD2 (total clearance: 0.505 vs -0.36 log ml/min/kg). Renal OCT2 substrate status was negative for both molecules, indicating no OCT2-associated substrate designation in the present output.

Toxicity predictions indicated several shared and distinct features. Both compounds were AMES-negative and hERG I inhibitor-negative, while hERG II inhibition was flagged for both. A notable divergence involved hepatotoxicity, predicted as negative for CPD2 and positive for Paclitaxel. Several quantitative toxicity indices were less favorable for CPD2 than for Paclitaxel. CPD2 showed a lower maximum tolerated dose (-0.085 vs 0.199 log mg/kg/day), a lower oral rat acute toxicity (LD50: 2.25 vs 2.776 mol/kg), and a lower oral rat chronic toxicity threshold (LOAEL: 1.76 vs 3.393 log mg/kg_bw/day). Ecotoxicity-related descriptors also differed, including *T. pyriformis* toxicity (0.864 vs. 0.285 log µg/L) and Minnow toxicity (-0.823 vs. 2.988 log mM).

Overall, CPD2 displays a mixed but potentially optimizable ADMET profile, with favorable predicted intestinal absorption, Caco-2 permeability, absence of CYP3A4 inhibition, and no hepatotoxicity alert. However, its limited aqueous solubility, reduced skin permeability, shared hERG II liability, higher predicted BBB/CNS permeability, and less favorable acute/chronic toxicity indices indicate key liabilities that should be addressed during lead optimization.

In contemporary drug discovery, Density Functional Theory (DFT) provides a practical quantum-chemical framework for describing molecular electronic structures and guiding compound design and optimization. Relative to many ab initio wavefunction methods, DFT provides a favorable compromise between chemical accuracy and computational expense, enabling practical application to chemically relevant systems [36]. DFT calculations were thus employed to complement the classical modeling results by characterizing the electronic structure and reactivity-associated descriptors of CPD2 relative to the reference compound, Paclitaxel. The computed parameters included EHOMO (eV), ELUMO (eV), ΔE (eV), μ (eV), χ (eV), η (eV), σ (eV-1), and ω (eV), which collectively summarize frontier-orbital energetics, resistance to charge redistribution, and electrophilic character (Table 4). Within this framework, EHOMO (eV) is commonly associated with electron-donating propensity, ELUMO (eV) reflects electron-accepting capacity, and ΔE (eV) (ELUMO - EHOMO) serves as an index of electronic stability versus chemical responsiveness.

Table 4: Quantum descriptors of CPD2 and Paclitaxel

Molecule	EHOMO (eV)	ELUMO (eV)	ΔE (eV)	μ (eV)	χ (eV)	η (eV)	σ (eV^{-1})	ω (eV)
CPD2	-7.2542	1.6480	8.9022	-2.8031	2.8031	4.4511	0.2247	0.8826
Paclitaxel	-8.6942	2.1568	10.8510	-3.2687	3.2687	5.4255	0.1843	0.9846

EHOMO (eV): highest occupied molecular orbitals; **ELUMO (eV)**: lowest unoccupied molecular orbitals; **ΔE (eV)**: energy gap; **μ (eV)**: chemical potential; **χ (eV)**: electronegativity; **η (eV)**: hardness; **σ (eV^{-1})**: softness; **ω (eV)**: electrophilicity index.

CPD2 exhibited EHOMO (eV) = -7.2542, higher than Paclitaxel (-8.6942), consistent with a comparatively greater tendency toward electron donation under the applied computational conditions. For ELUMO (eV), CPD2 presented a lower value (1.6480) than Paclitaxel (2.1568),

indicating a more accessible acceptor level for CPD2. Consequently, CPD2 displayed a smaller ΔE (eV) (8.9022) than Paclitaxel (10.8510), a pattern generally associated with increased electronic polarizability and higher chemical reactivity (Fig. 4). In contrast, the wider gap for Paclitaxel is consistent with enhanced frontier-orbital stability.

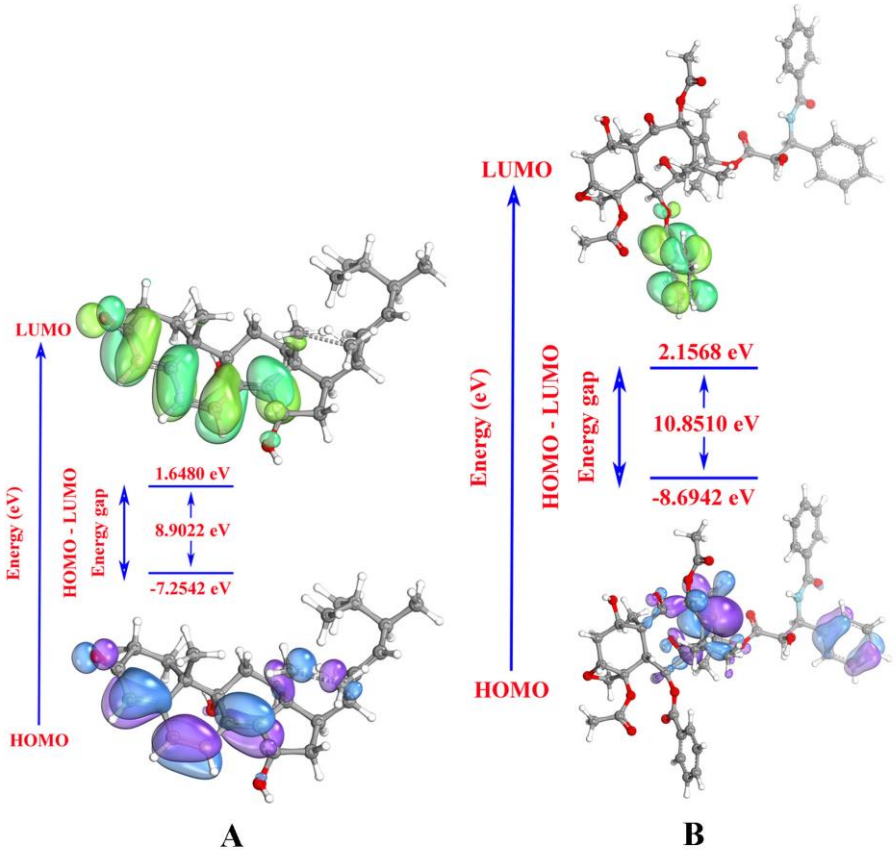

Figure 4: HOMO and LUMO surface diagrams of CPD2 (A) and Paclitaxel (B).

Global descriptors further differentiated the two molecules. Paclitaxel showed a higher χ (eV) (3.2687) than CPD2 (2.8031), accompanied by a more negative μ (eV) (-3.2687 vs -2.8031), indicating a stronger electron-attracting character for the reference ligand within this descriptor set. The hardness η (eV) was lower for CPD2 (4.4511) than for Paclitaxel (5.4255), with the reciprocal softness σ (eV^{-1}) correspondingly higher for CPD2 (0.2247) than for Paclitaxel (0.1843), supporting greater ease of electronic deformation for CPD2. Finally, ω (eV) was slightly lower for CPD2 (0.8826) than for Paclitaxel (0.9846), suggesting a marginally reduced electrophilicity index for CPD2 under the same theoretical level.

In conclusion, docking identified CPD2 as the leading ligand against Bcl-2/6O0K, showing a more favorable binding energy than Paclitaxel (-10.07 vs. -6.80 kcal/mol) and stable interactions within a conserved binding pocket. Molecular dynamics simulations supported the stability of the CPD2-6O0K complex over 100 ns, while MMGBSA analysis further favored CPD2 over Paclitaxel (-35.68 ± 2.88 vs. -29.75 ± 3.34 kcal/mol), mainly due to a lower solvation penalty.

ADMET profiling suggested favorable intestinal absorption, higher predicted clearance, and no hepatotoxicity alert for CPD2, although poor aqueous solubility and shared hERG II inhibition remain key liabilities. DFT descriptors further indicated greater electronic responsiveness for CPD2 relative to Paclitaxel. Notably, this study highlights the novelty of Talaromyces-derived steroids as underexplored fungal natural-product scaffolds for Bcl-2 inhibition, thereby providing a mechanistic rationale for their previously reported anti-HCC

potential. Overall, CPD2 emerges as a prioritized scaffold for Bcl-2 inhibition and HCC-oriented lead development. Future work should focus on experimental validation using Bcl-2-targeted biochemical assays, HCC cell-based apoptosis assays, and in vivo efficacy models. In parallel, structural optimization should aim to improve aqueous solubility, reduce hERG-related liability, and refine pharmacokinetic properties. Formulation strategies, such as solubilizing carriers or nanodelivery systems, may also be explored to overcome the predicted solubility limitation and enhance the translational potential of CPD2. Future in vitro and in vivo studies are required to validate these computational predictions and guide further lead optimization.

Conflict of Interest: The authors declare that there is no conflict of interest.

Authors' Contribution: Hung Duc Nguyen: the sole responsibility for the conception of the study, presented results and manuscript preparation. All data were generated in-house and that no paper mill was used.

Availability of data and material: The datasets used and/or analyzed during the current study are available from the corresponding author on reasonable request.

Funding: No funding was received for conducting this research.

REFERENCES

1. Bray F, Laversanne M, Sung H, Ferlay J, Siegel RL, Soerjomataram I, Jemal A. Global cancer statistics 2022: GLOBOCAN estimates of incidence and mortality worldwide for 36 cancers in 185 countries. CA Cancer J Clin 2024;74:229-263.
2. Tan EY, Danpanichkul P, Yong JN, Yu Z, Tan DJH, Lim WH, Koh B, Lim RYZ, Tham EKJ, Mitra K, Morishita A, Hsu YC, Yang JD, Takahashi H, Zheng MH, Nakajima A, Ng CH, Wijarnpreecha K, Muthiah MD, Singal AG, Huang DQ. Liver cancer in 2021: Global Burden of Disease study. J Hepatol 2025;82:851-860.
3. Liao W, Coupland CAC, Innes H, Jepsen P, Matthews PC, Campbell C; DeLIVER consortium; Barnes E, Hippisley-Cox J. Disparities in care and outcomes for primary liver cancer in England during 2008-2018: a cohort study of 8.52 million primary care population using the QResearch database. EClinicalMedicine 2023;59:101969.
4. Amin N, Anwar J, Sulaiman A, Naumova NN, Anwar N. Hepatocellular carcinoma: A comprehensive review. Diseases 2025;13:207.
5. Yoon JH, Choi SK. Management of early-stage hepatocellular carcinoma: challenges and strategies for optimal outcomes. J Liver Cancer 2023;23:300-315.
6. Cucchetti A, Elshaarawy O, Han G, Chong CCN, Serra C, O'Rourke JM, Crew R, Felicani C, Ercolani G, Shah T, Vogel A, Lai PBS, Johnson PJ. 'Potentially curative therapies' for hepatocellular carcinoma: how many patients can actually be cured? Br J Cancer 2023;128:1665-1671.
7. Wong RSY. Apoptosis in cancer: from pathogenesis to treatment. J Exp Clin Cancer Res 2011;30:87.
8. Campbell KJ, Tait SWG. Targeting BCL-2 regulated apoptosis in cancer. Open Biol 2018;8:180002.
9. Saddam M, Paul SK, Habib MA, Fahim MA, Mimi A, Islam S, Paul B, Helal MMU. Emerging biomarkers and potential therapeutics of the BCL-2 protein family: the apoptotic and anti-apoptotic context. Egypt J Med Hum Genet 2024;25:12.
10. Ma S, Chen GG, Lai PBS. Bcl-2 family members in hepatocellular carcinoma (HCC) - mechanisms and therapeutic potentials. In: Chen GG, Lai PBS (Eds), Apoptosis in Carcinogenesis and Chemotherapy: Apoptosis in Cancer. Springer Dordrecht 2009:219-235.

11. Roy A, Datta S, Bhatia KS, Bhumika, Jha P, Prasad R. Role of plant derived bioactive compounds against cancer. South African J Bot 2022;149:1017-1028.
12. Gupta A, Sathish Kumar B, Negi AS. Current status on development of steroids as anticancer agents. J Steroid Biochem Mol Biol 2013;137:242-270.
13. Zhang M, Deng Y, Liu F, Zheng M, Liang Y, Sun W, Li Q, Li XN, Qi C, Liu J, Chen C, Zhu H, Zhang Y. Five undescribed steroids from Talaromyces stipitatus and their cytotoxic activities against hepatoma cell lines. Phytochemistry 2021;189:112816.
14. Birkinshaw RW, Gong J, Luo CS, Lio D, White CA, Anderson MA, Blombery P, Lessene G, Majewski IJ, Thijssen R, Roberts AW, Huang DCS, Colman PM, Czabotar PE. Structures of BCL-2 in complex with venetoclax reveal the molecular basis of resistance mutations. Nat Commun 2019;10:2385.
15. Nguyen HD. Molecular docking and dynamic simulation of anti-apoptotic BCL-2 with saponins isolated from Weigela x "Bristol Ruby." Indian J Chem 2025;64:383-390.
16. Van Der Spoel D, Lindahl E, Hess B, Groenhof G, Mark AE, Berendsen HJC. GROMACS: Fast, flexible, and free. J Comput Chem 2005;26:1701-1718.
17. Guex N, Peitsch MC. SWISS-MODEL and the Swiss-Pdb Viewer: An environment for comparative protein modeling. Electrophoresis 1997;18:2714-2723.
18. Zoete V, Cuendet MA, Grosdidier A, Michielin O. SwissParam: A fast force field generation tool for small organic molecules. J Comput Chem 2011;32:2359-2368.
19. Pettersen EF, Goddard TD, Huang CC, Couch GS, Greenblatt DM, Meng EC, Ferrin TE. UCSF Chimera-A visualization system for exploratory research and analysis. J Comput Chem 2004;25:1605-1612.
20. Nguyen HD. Unveiling the anti-apoptotic mechanism of magnolialide as a colorectal cancer inhibitor via molecular modeling, ADMET, and MMGBSA analysis. Phys Chem Res 2025;13:783-796.
21. Neese F. Software Update: The ORCA program system-version 6.0. WIREs Comput Mol Sci 2025;15:e70019.
22. Knizia G, Klein JEMN. Electron flow in reaction mechanisms-revealed from first principles. Angew Chemie Int Ed 2015;54:5518-5522.
23. Hanwell MD, Curtis DE, Lonie DC, Vandermeersch T, Zurek E, Hutchison GR. Avogadro: an advanced semantic chemical editor, visualization, and analysis platform. J Cheminform 2012;4:17.
24. Luo J, Xue ZQ, Liu WM, Wu JL, Yang ZQ. Koopmans' theorem for large molecular systems within density functional theory. J Phys Chem A 2006;110:12005-12009.
25. Das R, Vigneresse JL, Chattaraj PK. Chemical reactivity through structure-stability landscape. Int J Quantum Chem 2014;114:1421-1429.
26. Agu PC, Afiukwa CA, Orji OU, Ezeh EM, Ofoke IH, Ogbu CO, Ugwuja EI, Aja PM. Molecular docking as a tool for the discovery of molecular targets of nutraceuticals in diseases management. Sci Rep 2023;13:13398.
27. Patil R, Das S, Stanley A, Yadav L, Sudhakar A, Varma AK. Optimized hydrophobic interactions and hydrogen bonding at the target-ligand interface leads the pathways of drug-designing. PLoS One 2010;5:e12029.
28. Bitencourt-Ferreira G, Veit-Acosta M, de Azevedo WF. Van der Waals potential in protein complexes. In: de Azevedo Jr WF (Ed), Docking screens for drug discovery. Springer New York 2019:79-91.
29. Salo-Ahen OMH, Alanko I, Bhadane R, Bonvin AMJJ, Honorato R V, Hossain S, Juffer AH, Kabedev A, Lahtela-Kakkonen M, Larsen AS, Lescrinier E, Marimuthu P, Mirza MU, Mustafa G, Nunes-Alves A, Pantsar T, Saadabadi A, Singaravelu K, Vanmeert M. Molecular dynamics simulations in drug discovery and pharmaceutical development. Processes 2021;9:71.
30. Lyle N, Das RK, Pappu RV. A quantitative measure for protein conformational heterogeneity. J Chem Phys 2013;139:121907.

31. Bornot A, Etchebest C, de Brevern AG. Predicting protein flexibility through the prediction of local structures. Proteins Struct Funct Bioinforma 2011;79:839-852.
32. Lobanov MY, Bogatyreva NS, Galzitskaya OV. Radius of gyration as an indicator of protein structure compactness. Mol Biol 2008;42:623-628.
33. Durham E, Dorr B, Woetzel N, Staritzbichler R, Meiler J. Solvent accessible surface area approximations for rapid and accurate protein structure prediction. J Mol Model 2009;15:1093-1108.
34. Dong L, Qu X, Zhao Y, Wang B. Prediction of binding free energy of protein-ligand complexes with a hybrid molecular mechanics/generalized born surface area and machine learning method. ACS Omega 2021;6:32938-32947.
35. Palagati S, Ramesh Reddy K, Satyanarayana SV, Garg T. Absorption, distribution, metabolism, excretion, and toxicity assessment of drugs using computational tools. In: Parihar A, Khan R, Kumar A, Kaushik AK, Gohel H (Eds), Computational approaches for novel therapeutic and diagnostic designing to mitigate SARS-CoV-2 infection. Academic Press Boston 2022:335-355.
36. Guan H, Sun H, Zhao X. Application of density functional theory to molecular engineering of pharmaceutical formulations. Int J Mol Sci 2025;26:3262.